Extreme Mechanics Letters 54 (2022) 101695

Contents lists available at ScienceDirect

Extreme Mechanics Letters

journal homepage: www.elsevier.com/locate/eml

Machine learning-based optimization of the design of composite pillars for dry adhesives

Aoyi Luo [a,*], Hang Zhang [b], Kevin T. Turner [a,*]

[a] Department of Mechanical Engineering and Applied Mechanics, University of Pennsylvania, Philadelphia, PA 19104-6315, USA
[b] Stuart Weitzman School of Design, University of Pennsylvania, Philadelphia, PA 19104-6315, USA

ARTICLE INFO

Article history:
Received 19 January 2022
Received in revised form 2 March 2022
Accepted 13 March 2022
Available online 25 March 2022

Keywords:
Adhesion
Interface failure
Machine learning
Optimization
Composite structure
Dry adhesive

ABSTRACT

A machine learning-based optimization strategy was used to find optimal designs for adhesive composite pillars with either high adhesion strength or high adhesion tunability. Neural networks were trained with data generated by finite element analysis to predict the adhesion strength of composite pillars with different designs; an average prediction error of less than 1% was achieved. Through a sensitivity study with the trained neural networks, it is found that the geometry of the stiff core above a critical cut off height has no effect on the interfacial stress distribution and the adhesion of the pillar. A randomly initialized constrained optimization algorithm was then applied to the trained neural networks to find the optimal composite pillar design. A composite pillar design with a stiff core that has an enlarged tapered flat end is optimal for realizing robust and high adhesion, since it can achieve high adhesion under different loading and contact conditions. The optimized pillar has a critical normal detachment force that is nearly 11 times that of a homogenous pillar and 1.7 times that of a composite pillar with a simple wide rectangular core under normal loading. A composite pillar with a thin flat stiff core shows the highest effective adhesion difference between being loaded with a normal force and being loaded with a moment.

1. Introduction

Dry adhesives that rely on van der Waals forces provide a route to realize robust, versatile and repeatable adhesion [1]. With their unparalleled capability, dry adhesives have found applications in microtransfer printing [2–4], wearable devices [5,6], climbing robots [7,8] and robotic grasping [9,10]. Since dry adhesives rely on secondary bonds such as van der Waals forces rather than specific chemical bonding, high adhesion strength is achieved through careful design of the adhesive structures. The geometry and elastic properties of the adhesive structure control the stress distribution at the adhered interface and thus can be designed to realize structures with high adhesive load capacity.

Mushroom-shaped pillars, inspired by the spatula-shaped tips of the setae on geckos' feet, have been the predominant design of dry adhesives for more than a decade. When a mushroom-shaped pillar is loaded, the interface stress is higher in the center of the contact and the stress concentration near the edge is lower compared to the interface stress distribution of a simple cylindrical pillar [11–14]. Such redistribution of the stress inhibits detachment initiated at the edge of the contact and results in enhanced load capacity [1,15]. In addition to mushroom-shaped pillars, composite pillars have been shown to have a favorable stress distribution compared to homogenous pillars. Composite pillars, consisting of a stiff core and a compliant tip also have a lower stress concentration at the edge and elevated stress in the center, and were predicted to and experimentally found to achieve enhanced adhesion relative to a homogenous pillar [16–19].

To realize the full potential of dry adhesion, design optimization of dry adhesive structures is essential. Extensive work has been done to optimize the geometry of mushroom-shaped pillars. Most of these efforts have used parametric studies within prescribed design spaces and finite element (FE) analysis to find the optimal dimensions [12,13,20,21]. Recently, Kim et al. [22] used a combination of deep learning and FE to predict the optimal shape of a single material pillar with a flared end. Son et al. [23] used a combination of Bayesian optimization and FE to determine the optimal design of a single material fibrillar adhesive, and experimentally fabricated and characterized the adhesion of the optimal design. For composite pillars, the adhesion of pillars with a simple core geometry and subjected to normal loading has been investigated [16,18,19,24], however, there are no optimization studies on the design of composite pillars for controlled adhesion under a broader range of loading conditions. In many applications, dry adhesives are subjected to a normal force as well as

* Corresponding authors.
E-mail addresses: luoaoyi@gmail.com (A. Luo), kturner@seas.upenn.edu (K.T. Turner).

https://doi.org/10.1016/j.eml.2022.101695
2352-4316/

other loading components (i.e., a shear force or an applied moment) due to factors such as the direction of the far-field applied load and misalignment. These non-normal loading components can significantly affect the detachment mechanism and adhesion strength of pillar structures [1,25,26]. Moreover, defects on the contact surface with unknown sizes (e.g., due to surface roughness, particles) can also play an important role in determining the detachment mechanism and effective adhesion strength of pillars [27]. To realize strong and robust dry adhesion, the geometry of composite pillars must be optimized to achieve high effective adhesion in all of these different loading and contact conditions. In addition, dry adhesive structures with high adhesion tunability, where the adhesion is strong under one loading condition but weak under another loading condition, are of interest for many pick-and-place applications. Thus, when considering the design and optimization of adhesive pillar structures, there is interest in identifying designs for both high adhesion strength and high adhesion tunability.

In this letter, a machine learning-based optimization approach is used to investigate the optimal design of the core geometry of composite pillars (Fig. 1(a)) with the highest effective adhesion strength under different loading and contact conditions. Moreover, the optimization framework is used to identify composite pillar designs with high adhesion tunability. This study is focused on 2D pillars in plane strain, which are representative of rectangular composite pillars. This geometry was chosen over an axisymmetric configuration because it allowed for the investigation of applied normal loads and moments via a 2D model. The 2D plane strain simulations of rectangular composite pillars under various loading conditions have significantly less computational cost than full 3D simulations, which would be needed to study circular composite pillars under multiple loading conditions. However, previous studies have shown that the interface stress distribution and adhesion strength of a circular axisymmetric composite pillar are comparable to a rectangular composite pillar with the same compliant tip layer thickness [19,24]. Thus, the results of this study are expected to provide insight into the design of circular composite pillars.

Machine learning and deep learning are increasingly being used in mechanical design because of their ability to correlate complex input to output and allow for the implementation of design optimization efficiently and accurately under various criteria [28–33]. The application of these techniques to mechanical design builds on extensive knowledge developed from application to problems in image processing [34] and speech recognition [35]. For optimization of the composite pillar design in this paper, neural networks (NNs) were trained with FE data to predict the effective adhesion strength and detachment mechanism of composite pillars under different conditions. A randomly initialized constrained optimization algorithm was then applied to the trained NNs to find the optimal composite pillar design with respect to different performance criteria.

2. Methods

2.1. Determination of adhesion strength and detachment mechanism

In this paper, two loading conditions are considered for the composite adhesive pillars, namely normal loading and moment loading as illustrated in Fig. 1(a) and (d). The effective adhesion strength under those two loading conditions is quantified by the critical normal force F_c^* or critical moment M_c^*, respectively. The goal of finding composite pillars with high adhesion is thus to find composite pillars with high F_c^* under normal loading or high M_c^* under moment loading. Composite adhesive pillars with high adhesion tunability are considered to be pillars that have high F_c^*/M_c^* (i.e., pillars with high F_c^* under normal loading and low M_c^* under moment loading). To calculate the adhesion strength, interface stress distributions for 25,920 unique composite pillar geometries under normal loading and moment loading conditions were first calculated by FE as described in the Supplementary Information. The composite pillars have an aspect ratio of 1 ($H = 2L$), and consist of a stiff core with Young's modulus $E_s = 2$ GPa, Poisson ratio $\nu_s = 0.3$ (representative of many thermoplastics and thermosets) and a compliant matrix with Young's modulus $E_c = 2$ MPa, Poisson ratio $\nu_c = 0.49$ (representative of common elastomers). The stiff core is limited to having either a flat or convex bottom surface and the compliant tip thickness is limited to $t_{min}/L \geq 0.2$ to ensure the tip layer is thick enough for fabrication, and good contact adaptability to the target surface in the presence of surface roughness and misalignment. The side profile of the core is described by a 6th order Bézier curve which is defined by seven control points (x_1,0.2L), (x_2,0.33L), (x_3,0.51L), (x_4,0.75L), (x_5,1.05L), (x_6,1.46L), (x_7,2.0L) (the expression of the Bézier curve is shown as eq. (S1)). The x-coordinates of the control points (x_1 to x_7) are varied to generate different side profile of the core and are constrained within the range [0.2L, 0.9L] to ensure that the stiff core has sufficient width to avoid fracture of the core and also that the stiff core does not extend to the edge of the pillar and separate the compliant shell into multiple disconnected regions, a geometry that would be difficult to fabricate. Example interface stress distributions are shown in Fig. 1. The calculated stress distributions are presented in normalized form. For the case of a composite pillar under normal loading, the normal stress distribution is normalized as $\sigma_{zz}/\overline{F}$, with

$$\overline{F} = \frac{b\int_{-L}^{L}\sigma_{zz}dx}{2bL} = \frac{F}{2bL}, \tag{1}$$

where b is the depth of the pillar. For the case of a composite pillar under moment loading, the normal stress distribution is normalized as $\sigma_{zz}/\overline{M}$, with

$$\overline{M} = \frac{b\int_{-L}^{L}\sigma_{zz}xdx}{2bL^2} = \frac{M}{2bL^2}. \tag{2}$$

For a composite pillar, there are two primary possible detachment mechanisms [16,18,19,24]. Detachment can initiate at either the edge of the contact or at a site within the contact (i.e. at the center or some other internal location). The detachment mechanism and adhesion strength of a composite pillar are determined by the size and location of the defects and stress distribution at the interface. Although the stress distribution calculated from FE described in Section 2.1 is the result of a perfectly bonded interface with no defect, the effective adhesion strength of an interface with defects can be inferred from this stress distribution when the defects are much smaller than the width of the pillar [4,12,19,36].

Consider an internal crack-like defect of size a_{in} (assuming $a_{in} \ll L$). The defect is a factor that affects the local adhesion of the interface [37,38], while it has negligible effect on the interfacial stress distribution on the pillar level. The critical stress σ_{in-c} that will lead to the growth of a crack-like defect of initial size a_{in} is [39]:

$$\sigma_{in-c} = \sqrt{\frac{\pi}{2}G_c E_c^* a_{in}}, \tag{3}$$

where G_c is the critical energy release rate and $E_c^* = E_c/(1\text{-}\nu_c^2)$. The critical normal force or moment to initiate failure from this defect is related to σ_{in-c} by the normalized stress distribution of this composite pillar. Assuming the size of the defects, a_{in}, is uniform over the internal region of the contact, the internal location with the highest stress will be the site where detachment

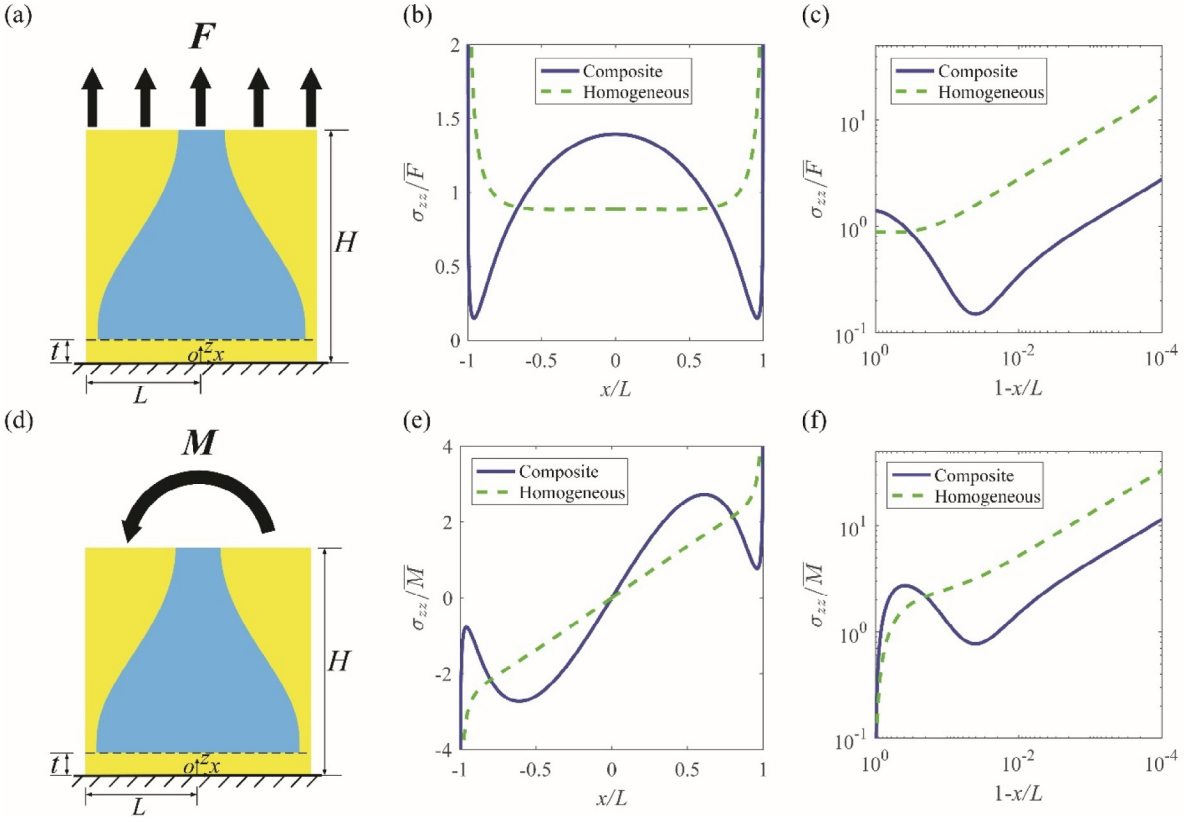

Fig. 1. (a) Schematic of a rectangular composite pillar in plane strain under normal loading which has $t/L = 0.2$ and $H/L = 2$. The core (blue) is 1,000 times stiffer than the shell (yellow). (b) Distribution of normal stress at the adhered interface for the composite pillar shown in Fig. 1(a) and a homogenous pillar (i.e., no stiff core) under normal loading. Note, the maximum stress on the y-axis is truncated at 2. (c) Normal stress at the adhered interface near the edge for the composite pillar and a homogenous pillar under normal loading. (d) Schematic of a rectangular composite pillar in plane strain under moment loading. (e) Distribution of normal stress at the adhered interface for the composite pillar as shown in Fig. 1(d) and a homogenous pillar under moment loading (the y-axis is truncated at ± 4). (f) Normal stress at the adhered interface near the edge for the composite pillar and a homogenous pillar under moment loading. (For interpretation of the references to color in this figure legend, the reader is referred to the web version of this article.)

initiates and will determine the critical normal force or critical moment for cases where failure initiates within the contact. For a normal loading case, the critical normal force F_{in-c} corresponding to failure from a small internal defect is:

$$\frac{F_{in-c}}{2bL} = \frac{\sigma_{in-c}}{\sigma_{in-max}/\overline{F}}, \tag{4}$$

where σ_{in-c} is calculated by Eq. (3) and $\sigma_{in-max}/\overline{F}$ is the normalized internal peak stress. Similarly, for the moment loading case, the critical moment M_{in-c} corresponding to failure from an internal defect is:

$$\frac{M_{in-c}}{2bL^2} = \frac{\sigma_{in-c}}{\sigma_{in-max}/\overline{M}}. \tag{5}$$

However, failure can initiate from an edge also. For the composite pillar geometry studied, there is a stress concentration at the edge of the contact. At the edge, there is a stress singularity $\sigma_{zz} = H_s(L-x)^{-0.41}$, where H_s is the magnitude of singularity and $(L\text{-}x)$ is the distance from the edge [19]. Assuming that the edge defect with size a_{edge} is much smaller than the width of the pillar (such that it is embedded within the stress singularity dominated region near the edge), the critical magnitude of singularity at the edge, H_c, is [19]

$$H_c = \sqrt{\frac{G_c E_c^* a_{edge}^{-0.20}}{3.7}}. \tag{6}$$

The critical external normal force to initiate failure from the edge is thus

$$\frac{F_{edge-c}}{2bL} = \frac{H_c}{H_N^*}, \tag{7}$$

where H_N^* is the normalized magnitude of singularity at the edge obtained from the normalized stress distribution $\sigma_{zz}/\overline{F}$. H_N^* is the intercept of the linear region in a logarithmic plot of the normalized stress distribution (e.g., linear region in Fig. 1(c)) [19] and is obtained from the FE calculations. Similarly, the critical external moment to initiate failure from an edge defect can be calculated as

$$\frac{M_{edge-c}}{2bL^2} = \frac{H_c}{H_M^*}. \tag{8}$$

The effective adhesion strength and the location where detachment initiates are determined by the defect at the interface that leads to the lowest critical force or moment. Whether a composite pillar detaches from an internal defect or an edge defect, as well as the critical normal force F_c (or the critical moment M_c), are determined by the smaller of F_{in-c} and F_{edge-c} for normal loading (and smaller of M_{in-c} and M_{edge-c} for moment loading). Both F_{in-c} and F_{edge-c} depend on the defect sizes, but the exact value of a_{in} and a_{edge} are application dependent, since they are affected by various factors such as material properties, fabrication precision, cleanliness, and substrate roughness. As the defect sizes are, in general unknown, in this design study we assume $a = a_{in} = a_{edge}$ throughout the study. With this assumption, the detachment

mechanism is determined by the following ratios:

$$\frac{F_{in-c}}{F_{edge-c}} = 2.2a^{-0.4}\frac{H_N^*}{\sigma_{in}/\overline{F}} \tag{9}$$

under normal loading or

$$\frac{M_{in-c}}{M_{edge-c}} = 2.2a^{-0.4}\frac{H_M^*}{\sigma_{in}/\overline{M}} \tag{10}$$

under moment loading. Edge detachment is expected for cases where these ratios are greater than 1 and internal crack initiation is expected for ratios less than 1. We investigated two defect sizes, $a/L = 0.001$ and $a/L = 0.005$, to demonstrate the effect of defect size on the optimal design. The optimization results for other a/L can be easily obtained as long as the assumption that the defect is sufficiently small compared to the width of the pillar holds. The critical normal force and moment are reported in nondimensional forms:

$$F_c^* = \frac{F_c}{2b\sqrt{G_c E_c^* L}}, \tag{11}$$

$$M_c^* = \frac{M_c}{2bL\sqrt{G_c E_c^* L}}. \tag{12}$$

2.2. Neural networks

Machine learning calculations were conducted using TensorFlow [40]. Four fully connected neural networks were constructed to predict the effective adhesion strength of composite pillars under 4 different conditions (i.e., under normal loading or moment loading with $a/L = 0.001$ or $a/L = 0.005$), as the schematic Fig. S1(a) shows. The positions of the control points (x_1 to x_7) are inputs to the NNs and represent the geometry of the composite pillar, and the effective adhesion strength (F_c^* or M_c^*) is the output. The NNs consist of multiple fully connected layers: an input layer with 7 scalar inputs, an output layer with 1 scalar output, and 2 hidden layers with 64/16 neurons. 25,920 different pillar geometries were examined in FE, which generated 25,920 data pairs for each NN. 90% of the data was selected randomly as the training set, while the remaining 10% data was the validation set. A stochastic gradient descent optimizer "Adam" was used. "ReLu" was chosen as the activation function, and mean square error was chosen as the loss function [41].

Five different NN structures with varied depth and neuron number were evaluated based on mean absolute percentage error for the 4 different conditions (the structures and prediction errors of those NNs are summarized in Fig. S1(b) and (c)). The NN structure with 2 hidden layers and 64/16 neurons had the lowest mean absolute percentage error and was then used throughout the study for prediction and optimization.

Besides the four NNs trained to predict effective adhesion of the pillars, two binary classification NNs were constructed to predict the detachment mechanism (edge detachment or internal detachment) of the pillars under normal loading with $a/L = 0.001$ or $a/L = 0.005$, as described in the Supplementary Information.

2.3. Optimization

A trained NN with all weights and biases fixed is equivalent to an algebraic function and its derivatives can be calculated analytically, so optimization algorithms that find the extremum values of a function can be used to find the extremum outputs of the trained NNs and the corresponding inputs [42–44]. Constrained minimization algorithm trust-region constrained method from Python SciPy library was used to perform optimization on the 4 NNs that were trained to predict the effective adhesion. As a minimization algorithm, maximization was performed by minimizing the negative value of the function output. The input variables x_1 to x_7 were constrained within the range $[0.2L, 0.9L]$ in the optimization. Since the quasi-Newton based optimization algorithm may converge to a local extremum values depending on the initial point of search, the optimization algorithm was run 100 times with a random initial point each time to generate 100 candidate geometries that have local optimal performances. The final optimized design was chosen to be the best one among the 100 local optimal candidates. Note that in our study, at least the top 3 candidates have the same geometry. The duplication of the best design generated by randomly initialized optimizations indicates 100 optimum searches are very likely to capture all the local optimum and are able to predict the global optimum.

3. Results and discussion

The stress distributions of a composite pillar in plane strain under normal loading and moment loading as shown in Fig. 1(a) and (d) are summarized in Fig. 1 to provide insight into the basic mechanics of these structures. The stress distributions for a simple homogenous pillar are also shown for comparison. When a composite pillar is subjected to a normal force (Fig. 1(a)), the stress in the center region of the contact is elevated compared to a homogenous pillar due to the presence of a stiff core (Fig. 1(b)). By equilibrium, the stress near the edge is thus reduced compared to a homogenous pillar. To highlight the details of the stress distribution and singularity near the edge, the stress distribution is replotted on a logarithmic scale (Fig. 1(c)). The linear region in this logarithmic plot is the edge singularity dominated region, and the intercept is log H_N^*. Fig. 1(c) clearly shows that the stress near the edge and the magnitude of singularity (H_N^*) are reduced in the composite design — this inhibits edge initiated detachment and increases the critical normal force F_c^* relative to a homogenous pillar. However, since the effective adhesion strength of an interface is determined by the location where detachment first initiates, elevating the internal stress too much can shift crack initiation from the edge to an internal site and reduce the adhesion [24]. As a result, the optimal adhesion cannot be achieved by solely reducing the stress at one position, and an optimized result that balances the stress distribution over the entire contact area is needed.

In many applications, an adhesive pillar is subjected to a shear force and/or moment in addition to a normal force due to factors such as misalignment, surface non-flatness, and far-field loads with varying directions [1,25,26]. Moreover, a shear force or moment can be applied intentionally to actively reduce the adhesion of a pillar for easy release [16,17,45]. It is thus important to consider additional loading conditions. When a shear force is applied to the top of an adhesive pillar, its effect on the interfacial stress distribution is primarily through the moment generated by this shear force rather than the shear stress introduced at the interface, because an adhesive pillar typically has a high aspect ratio and thus a long moment arm for the shear force to act over [4]. Moreover, a moment contributes to mode I failure which is the lowest energy failure mode, while shear stresses contribute to mode II failure. As a result, we focus on the moment loading case as shown in (Fig. 1(d)). When a moment is applied to a composite pillar, different from a homogenous pillar where the stress varies monotonically from one edge to the other edge of the contact, a peak in the tensile stress distribution within the interior of the contact is observed because of the stiff core (Fig. 1(e)), and the magnitude of the stress near the edge is reduced (Fig. 1(f)).

To find the optimal composite pillar designs under different conditions, 4 separate NNs were first trained to predict the critical

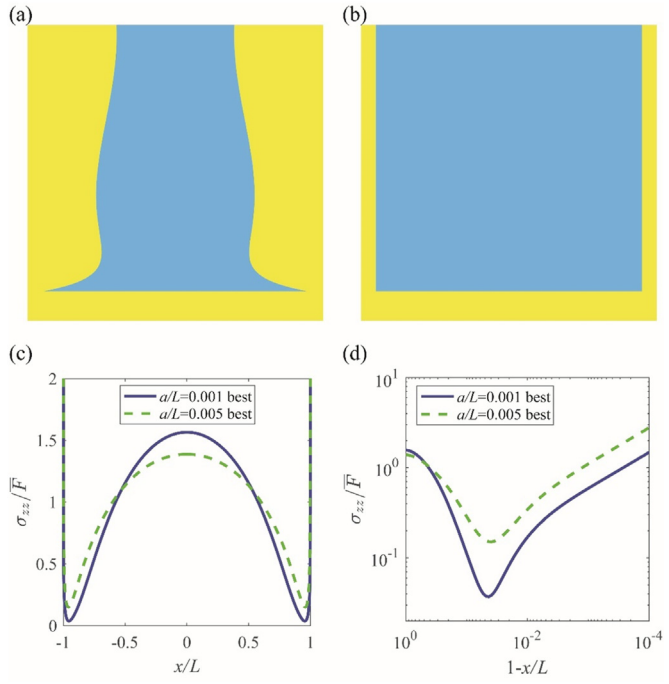

Fig. 2. The optimal composite pillar designs for different crack lengths under normal loading (the core (blue) is 1,000 times stiffer than the shell (yellow)). (a) The optimal design with $a/L = 0.001$. (b) The optimal design with $a/L = 0.005$. (c) Normal stress at the adhered interface for these two designs (the maximum value of the y-axis is truncated at 2). (d) Normal stress at the adhered interface near the edge for these two designs. (For interpretation of the references to color in this figure legend, the reader is referred to the web version of this article.)

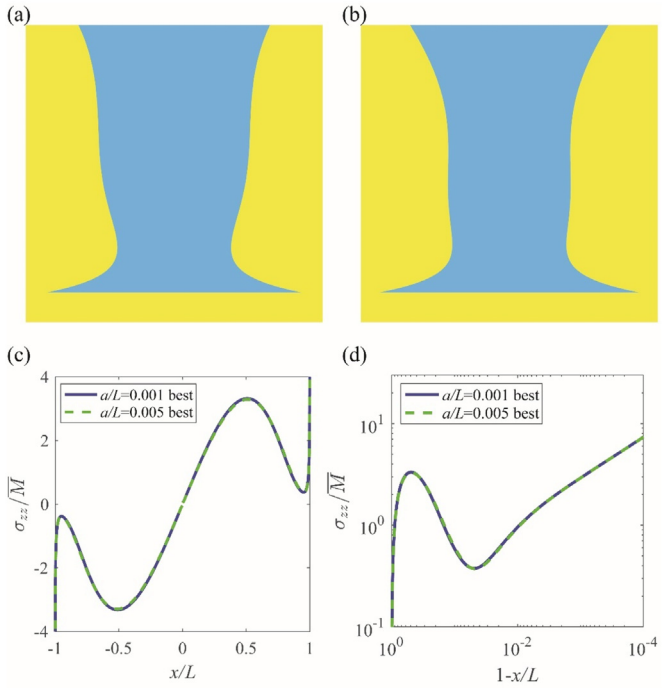

Fig. 3. The optimal composite pillar designs for different crack lengths under moment loading (the core (blue) is 1,000 times stiffer than the shell (yellow)). (a) The optimal design with $a/L = 0.001$. (b) The optimal design with $a/L = 0.005$. (c) Normal stress at the adhered interface for these two designs (the maximum value of the y-axis is truncated at ± 4). (d) Normal stress at the adhered interface near the edge for these two designs. (For interpretation of the references to color in this figure legend, the reader is referred to the web version of this article.)

normal force F_c^* or the critical moment M_c^* of a composite pillar with defect size $a/L = 0.001$ or $a/L = 0.005$. Input data to the NNs are the positions of the control points of Bézier curve, x_1 to x_7, that describe the shape of the stiff core. The output is F_c^* or M_c^* of the pillar with $a/L = 0.001$ or $a/L = 0.005$. After NNs were trained, a randomly initiated constrained optimization algorithm was applied to those NNs to find the maximum output and the corresponding input with respect to different criteria. In addition to the NNs used to predict F_c^* and M_c^*, binary classifiers were also built to predict the detachment mechanism of the composite pillars under normal loading (i.e., whether the detachment is initiated at edge or internal region of the contact). Note that for the moment loading case, all of the composite pillars investigated detach from the edge, so there is no need to build a binary classifier for moment loading cases.

The optimal composite pillar designs that have the highest critical normal force F_c^* with defect size $a/L = 0.001$ or $a/L = 0.005$ are first investigated using the machine learning-based optimization algorithm, and the results are summarized in Fig. 2 and Table S2. The predicted optimal design that has the highest F_c^* assuming $a/L = 0.001$ (Fig. 2(a)) is different from the predicted optimal design assuming $a/L = 0.005$ (Fig. 2(b)), which is simply the case with the widest rectangular core ($x_i/L = 0.90$). To understand the reason for this difference, stress distributions of the two designs are shown in Fig. 2(c) and (d). The optimal design with $a/L = 0.001$ has a more slender core than the optimal design with $a/L = 0.005$, thus the stress is higher in the center of the contact and lower near the edge for the $a/L = 0.001$ optimal case. According to Eq. (9) and Fig. S2, when the defect size a/L is smaller, edge detachment is more favorable compared to detachment initiated at an internal site, so the optimal design with $a/L = 0.001$ tends to reduce the stress near the edge more than that of the optimal design with $a/L = 0.005$ to suppress the edge detachment. As the results in Fig. S2(c) and Table S2 indicate, when $a/L = 0.001$, the composite pillar design shown in Fig. 2(a) with an a/L of 0.001 has a critical normal force that is 11.2× that of a homogenous pillar with an a/L of 0.001 and 1.7× that of the composite pillar design shown in Fig. 2(b) assuming the same crack size $a/L = 0.001$. When $a/L = 0.005$, the composite pillar design shown in Fig. 2(b) with an a/L of 0.005 achieves a critical normal force that is 6.5×that of a homogenous pillar with an a/L of 0.005 and 10% higher than that of the composite pillar design shown in Fig. 2(a) assuming the same crack size $a/L = 0.005$. Results in Fig. 2 demonstrate that the optimal design can vary as the defect size varies, and there may not be a universal optimal composite pillar design under different contact conditions on various surfaces.

The optimal composite pillar designs that have the highest critical moment M_c^* with defect size $a/L = 0.001$ or $a/L = 0.005$ were also determined. As all moment-loaded pillars fail from the edge that experiences tension, it is expected that the optimal design should be the one with the lowest magnitude of edge stress (i.e., the lowest H_M^* in Eq. (8)) for both $a/L = 0.001$ and $a/L = 0.005$. The optimized designs are shown in Fig. 3(a) and (b) and Table S3. The first three control points (x_1 to x_3) of these two optimal designs are nearly the same and the rest of the control points are different (x_4 to x_7), yet their interface stress distributions are the same (Fig. 3(c) and (d)). The critical moment is 4.5× that of a homogenous pillar and 1.5× that of a composite pillar with the widest rectangular core investigated ($x_i/L = 0.90$). With the trained NNs, a sensitivity study was conducted to help understand the effect of the position of each control point on the critical normal force and moment, and the results are summarized in Fig. 4. As the control point is further away from the adhered interface, its effect on the critical force and moment

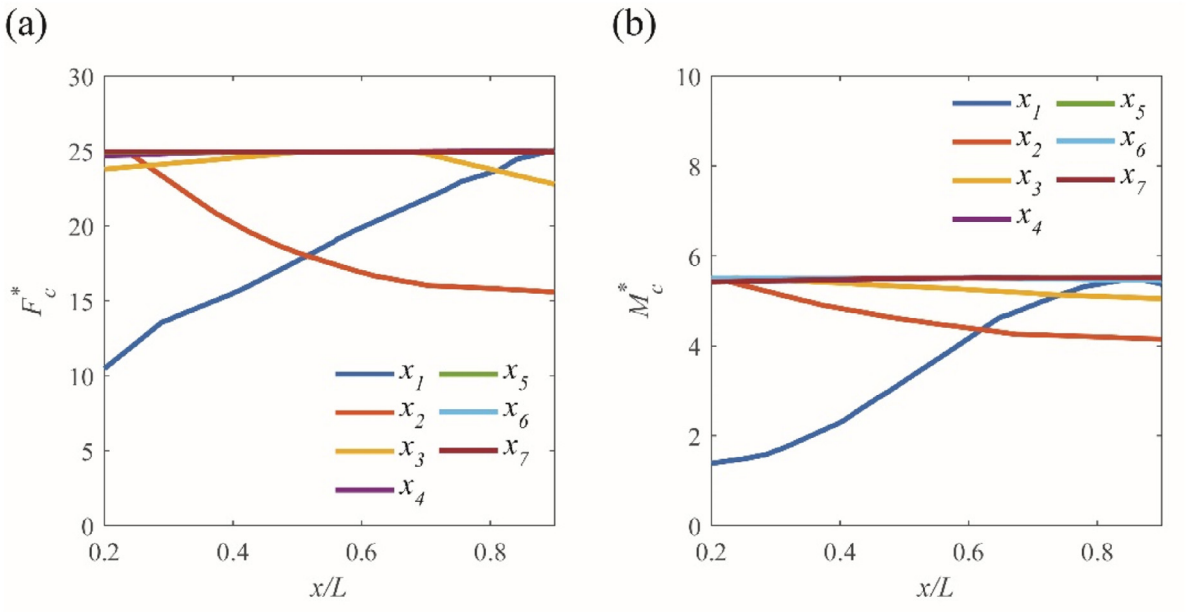

Fig. 4. (a) The critical normal force F_c^* as a function of each control point position. Each curve corresponds to varying the position of one control point with other control points kept the same as the design in Fig. 2(a). The critical moment M_c^* as a function of each control point position. Each curve corresponds to varying the position of one control point with other control points kept the same as the design in Fig. 3(a).

becomes smaller, which is expected according to Saint-Venant's principle. Only the position of the first three control points affects critical force and moment, and the position of the first two control points are the dominant ones. This explains why the designs in Fig. 3(a) and (b) have the same stress distributions even though only x_1 to x_3 to are similar. Note that x_1 and x_2 for the designs in Fig. 3(a) and (b) are also almost the same as those for the design in Fig. 2(a), which indicates those designs are able to achieve high adhesion under both normal and moment loading conditions. This observation also provides a cut-off height for the design of composite pillars for which the structure and detail distribution of the external loading above this cut-off height $z/L \geq 0.51$ have no effect on the interfacial stress distribution and effective adhesion.

With the NNs, we can identify the optimal composite pillar design under more complicated criteria. We have shown in Fig. 2 that the optimal design under normal loading depends on the defect size. However, the defect size for an adhesive pillar in contact with various surfaces is typically unknown. It is thus useful to perform optimization based on a criterion that accounts for the performance of the adhesive pillar with multiple possible defect sizes. As a demonstration here, a criterion that seeks the optimal design which maximizes the sum of the critical normal forces under both $a/L = 0.001$ and $a/L = 0.005$ is defined as:

$$\frac{F_c^*\,(a/L = 0.001)}{F_{c-max}^* F\,(a/L = 0.001)} + \frac{F_c^*\,(a/L = 0.005)}{F_{c-max}^*\,(a/L = 0.005)}, \tag{13}$$

where $F_{c-max}^*(a/L = 0.001)$ and $F_{c-max}^*(a/L = 0.005)$ are normalization factors, $F_{c-max}^*(a/L = 0.001)$ is the critical normal force achieved by the design shown in Fig. 2(a) with $a/L = 0.001$ and $F_{c-max}^*(a/L = 0.005)$ is the critical normal force achieved by the design shown in Fig. 2(b) with $a/L = 0.005$. The optimal design that maximizes Eq. (13) is shown in Fig. 5(a) and Table S4. The effective control points (x_1 to x_3) are almost the same as those of the design shown in Fig. 2(a). As Fig. S2(c) shows, though the design in Fig. 2(a) has a F_c^* 10% lower than the design in Fig. 2(b) with a relatively large defect size ($a/L = 0.005$), it has a F_c^* 72% higher when the defect is smaller ($a/L = 0.001$). As the criterion is based on the sum of F_c^* for both $a/L = 0.001$ and $a/L = 0.005$, the design in Fig. 2(a) is predicted to be the optimal design.

In real applications, adhesive pillars often need to work under different loading conditions, and it is often desirable to have high adhesion under both normal loading and moment loading conditions. To find a composite pillar design with high adhesion under both loading conditions, we propose a criterion that maximizes the sum of the critical normal force and moment:

$$\frac{F_c^*}{F_{c-max}^*} + \frac{M_c^*}{M_{c-max}^*}. \tag{14}$$

To demonstrate this criterion, we choose $a/L = 0.001$ and F_{c-max}^* is the critical normal force achieved by the design shown in Fig. 2(a) with $a/L = 0.001$, and M_{c-max}^* is the critical moment achieved by the design shown in Fig. 3(a) with $a/L = 0.001$. The corresponding optimal design is shown in Fig. 5(b) and Table S5. The effective control points (x_1 to x_3) are also very similar to those of the design shown in Fig. 2(a). The designs in Fig. 5(a) and (b) suggest that the design in Fig. 2(a), where the stiff core has an flat enlarged tapered end, is the optimal design for robust and high adhesion since it maximizes the sum of the adhesion capacity with two defect sizes and two different loading conditions.

In addition to pillars with robust and strong adhesion, pick-and-place applications often require adhesive pillars to have high adhesion tunability, i.e., an adhesion strength that is high under normal loading and low under moment (or shear) loading. To maximize the adhesion tunability, we maximize the adhesion switching ratio, which is the ratio of the critical normal force to the critical moment:

$$\frac{F_c^*/F_{c-max}^*}{M_c^*/M_{c-max}^*}. \tag{15}$$

Again, $a/L = 0.001$ is chosen to demonstrate this criterion here. The composite pillar with the thinnest stiff core ($x_i/L = 0.20$) within the range investigated as shown in Fig. 5(c) and Table S6 has the highest adhesion switching ratio. It achieves a switching ratio that is 4.7× that of a homogenous pillar and 2.1× that of the composite pillar with the widest rectangular core ($x_i/L = 0.90$) (Fig. 2(b)). The composite pillar with the thinnest rectangular core ($x_i/L = 0.20$) exhibits higher adhesion tunability compared with the composite pillar with the widest rectangular

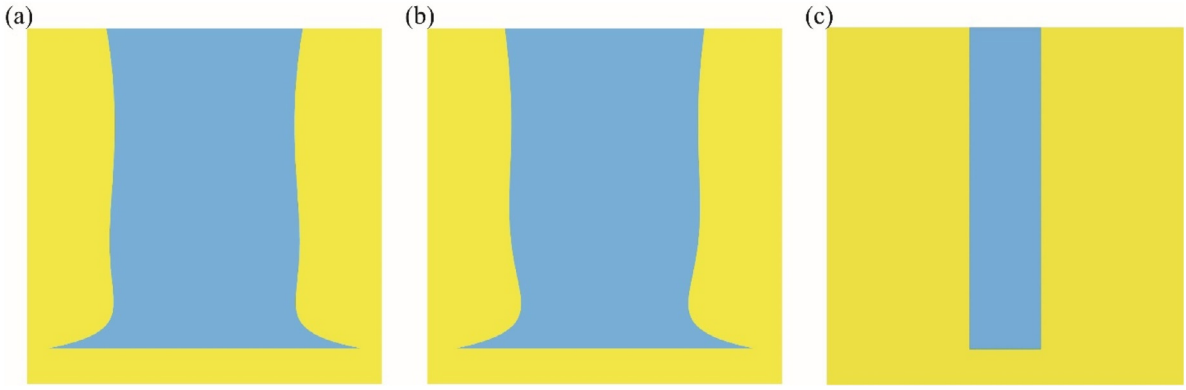

Fig. 5. The optimal composite pillar designs under different criteria (the core (blue) is 1,000 times stiffer than the shell (yellow)). (a) The design that achieves highest F_c^*/F_{c-max}^* with $a/L = 0.001$ + F_c^*/F_{c-max}^* with $a/L = 0.005$. (b) The design that achieves highest F_c^*/F_{c-max}^*+ M_c^*/M_{c-max}^* with $a/L = 0.001$. (c) The design that achieves highest $(F_c^*/F_{c-max}^*)/(M_c^*/M_{c-max}^*)$ with $a\ /L = 0.001$. (For interpretation of the references to color in this figure legend, the reader is referred to the web version of this article.)

core ($x_i/L = 0.90$) because its critical normal force is 22% lower while its critical moment is 58% lower than the composite pillar with the widest core. Since a pillar is more likely to fail from the edge when the crack size is small ($a/L = 0.001$ here), even though there is a high stress in the center of the contact for the composite pillar with the thinnest core ($x_i/L = 0.20$), it still fails from the edge and the magnitude of the stress near the edge is 27% higher than the composite pillar with the widest core (Fig. S3(a) and (b)). However, when loaded with a moment, the position of the internal peak stress of the composite pillar with thinnest core is closer to the center of the contact compared to the position of the internal peak stress of the composite pillar with widest core, and its internal peak stress thus generates less moment. As a result, for a given total moment, the magnitude of the stress near the edge for the composite pillar with the thinnest core is 2.4×that of the composite pillar with the widest core (Fig. S3(c) and (d)). It should be noted that a composite pillar design generally cannot achieve robust high adhesion (which requires the adhesion to be high under all loading conditions) and high adhesion tunability (which requires the adhesion to be low under at least one specific loading condition) simultaneously. The high adhesion tunability of the design shown in Fig. 5(c) is achieved by compromising its adhesion strength under both normal and moment loading conditions compared to the design shown in Fig. 5(b) (F_c^* is 53% lower and M_c^* is 76% lower for the design shown in Fig. 5(c) compared to the design shown in Fig. 5(b)).

4. Conclusion

In this study, we investigated the optimal design of adhesive composite pillars with high effective adhesion strength under different loading and contact conditions through a machine learning-based approach. The composite pillar design with the highest adhesion tunability through different loading modes was also studied. Neural networks were trained with data generated by finite element analysis to predict the adhesion strength of different composite pillar designs, and then used to find the optimal design with the best performance. It is found that the geometry of the stiff core above the critical cut off height $z/L \geq 0.51$ has no effect on the interfacial stress distribution and effective adhesion strength. Moreover, we find the optimal design depends on the loading condition and the size of defects at the interface. Optimization based on combined criteria that account for the adhesion of composite pillars under different conditions together was then conducted. The composite pillar design with a stiff core that has an enlarged tapered end with a flat bottom surface is found to be the optimal design for robust and high adhesion, as it can achieve high adhesion with different loading and contact conditions. A composite pillar with a thin flat bottom core exhibits high adhesion switching ratio that enables large adhesion tunability for easy release. These optimizations demonstrate the ability of machine learning to optimize mechanical structure design efficiently and quickly under complicated combined criterion.

CRediT authorship contribution statement

Aoyi Luo: Conceptualization, Formal analysis, Investigation, Validation, Writing – original draft, Writing – review & editing. **Hang Zhang:** Formal analysis, Writing – original draft. **Kevin T. Turner:** Conceptualization, Supervision, Writing – review & editing.

Declaration of competing interest

The authors declare the following financial interests/personal relationships which may be considered as potential competing interests: Kevin T. Turner is an inventor on a related patent, #US 10,549,483 B2, that is assigned to Trustees of the University of Pennsylvania.

Acknowledgments

Aoyi Luo and Kevin T. Turner gratefully acknowledge support from National Science Foundation, USA under awards CMMI 1663037 and CMMI 1761726. The authors thank Sumukh Shankar Pande for providing helpful discussion on the Bézier curve.

Appendix A. Supplementary data

Supplementary information (SI) related to this article can be found online at https://doi.org/10.1016/j.eml.2022.101695. The SI includes additional detail on the methods, data for specific designs in tabular form, and supplementary plots that enhance understanding of the primary results in the letter.

References

[1] R. Hensel, K. Moh, E. Arzt, Engineering micropatterned dry adhesives: From contact theory to handling applications, Adv. Funct. Mater. 28 (2018) 1800865, http://dx.doi.org/10.1002/adfm.201800865.
[2] A. Carlson, S. Wang, P. Elvikis, P.M. Ferreira, Y. Huang, J.A. Rogers, Active, programmable elastomeric surfaces with tunable adhesion for deterministic assembly by transfer printing, Adv. Funct. Mater. 22 (2012) 4476–4484, http://dx.doi.org/10.1002/adfm.201201023.

[3] H.J. Kim-Lee, A. Carlson, D.S. Grierson, J.A. Rogers, K.T. Turner, Interface mechanics of adhesiveless microtransfer printing processes, J. Appl. Phys. 115 (2014) 104066, http://dx.doi.org/10.1063/1.4870873.
[4] A. Luo, K.T. Turner, Mechanics of crack path selection in microtransfer printing: Challenges and opportunities for process control, J. Mech. Phys. Solids 143 (2020) 104066, http://dx.doi.org/10.1016/j.jmps.2020.104066.
[5] D.M. Drotlef, M. Amjadi, M. Yunusa, M. Sitti, Bioinspired composite microfibers for skin adhesion and signal amplification of wearable sensors, Adv. Mater. 29 (2017) 1–8, http://dx.doi.org/10.1002/adma.201701353.
[6] D.H. Kim, N. Lu, R. Ma, Y.S. Kim, R.H. Kim, S. Wang, J. Wu, S.M. Won, H. Tao, A. Islam, K.J. Yu, T. Il Kim, R. Chowdhury, M. Ying, L. Xu, M. Li, H.J. Chung, H. Keum, M. McCormick, P. Liu, Y.W. Zhang, F.G. Omenetto, Y. Huang, T. Coleman, J.A. Rogers, Epidermal electronics, Science 333 (2011) 838–843, http://dx.doi.org/10.1126/science.1206157.
[7] M.T. Pope, C.W. Kimes, H. Jiang, E.W. Hawkes, M.A. Estrada, C.F. Kerst, W.R.T. Roderick, A.K. Han, D.L. Christensen, M.R. Cutkosky, A multimodal robot for perching and climbing on vertical outdoor surfaces, IEEE Trans. Robot. 33 (2017) 38–48, http://dx.doi.org/10.1109/TRO.2016.2623346.
[8] B. Aksak, M.P. Murphy, M. Sitti, Gecko inspired micro-fibrillar adhesives for wall climbing robots on micro/nanoscale rough surfaces, in: Proc. - IEEE Int. Conf. Robot. Autom., 2008, pp. 3058–3063, http://dx.doi.org/10.1109/ROBOT.2008.4543675.
[9] S. Song, Di.M. Drotlef, C. Majidi, M. Sitti, Controllable load sharing for soft adhesive interfaces on three-dimensional surfaces, Proc. Natl. Acad. Sci. USA 114 (2017) E4344–E4353, http://dx.doi.org/10.1073/pnas.1620344114.
[10] E.W. Hawkes, H. Jiang, D.L. Christensen, A.K. Han, M.R. Cutkosky, Grasping without squeezing: Design and modeling of shear-activated grippers, IEEE Trans. Robot. 34 (2018) 303–316, http://dx.doi.org/10.1109/TRO.2017.2776312.
[11] G. Carbone, E. Pierro, S.N. Gorb, Origin of the superior adhesive performance of mushroom-shaped microstructured surfaces, Soft Matter 7 (2011) 5545–5552, http://dx.doi.org/10.1039/c0sm01482.
[12] R.G. Balijepalli, M.R. Begley, N.A. Fleck, R.M. McMeeking, E. Arzt, Numerical simulation of the edge stress singularity and the adhesion strength for compliant mushroom fibrils adhered to rigid substrates, Int. J. Solids Struct. 85–86 (2016) 160–171, http://dx.doi.org/10.1016/j.ijsolstr.2016.02.018f.
[13] B. Aksak, K. Sahin, M. Sitti, The optimal shape of elastomer mushroom-like fibers for high and robust adhesion, Beilstein J. Nanotechnol. 5 (2014) 630–638, http://dx.doi.org/10.3762/bjnano.5.74.
[14] V. Liimatainen, D.M. Drotlef, D. Son, M. Sitti, Liquid-superrepellent bioinspired fibrillar adhesives, Adv. Mater. 32 (2020) 2000497, http://dx.doi.org/10.1002/adma.202000497.
[15] S. Kim, A. Carlson, H. Cheng, S. Lee, J.K. Park, Y. Huang, J.A. Rogers, Enhanced adhesion with pedestal-shaped elastomeric stamps for transfer printing, Appl. Phys. Lett. 100 (2012) 171909, http://dx.doi.org/10.1063/1.4706257.
[16] H.K. Minsky, K.T. Turner, Achieving enhanced and tunable adhesion via composite posts, Appl. Phys. Lett. 106 (2015) 201604, http://dx.doi.org/10.1063/1.4921423.
[17] H.K. Minsky, K.T. Turner, Composite microposts with high dry adhesion strength, ACS Appl. Mater. Interfaces 9 (2017) 18322–18327, http://dx.doi.org/10.1021/acsami.7b01491.
[18] S.C.L. Fischer, E. Arzt, R. Hensel, Composite pillars with a tunable interface for adhesion to rough substrates, ACS Appl. Mater. Interfaces 9 (2017) 1036–1044, http://dx.doi.org/10.1021/acsami.6b11642.
[19] R.G. Balijepalli, S.C.L. Fischer, R. Hensel, R.M. McMeeking, E. Arzt, Numerical study of adhesion enhancement by composite fibrils with soft tip layers, J. Mech. Phys. Solids 99 (2017) 357–378, http://dx.doi.org/10.1016/j.jmps.2016.11.017.
[20] G. Carbone, E. Pierro, Sticky bio-inspired micropillars: Finding the best shape, Small 8 (2012) 1449–1454, http://dx.doi.org/10.1002/smll.201102021.
[21] X. Zhang, Y. Wang, R. Hensel, E. Arzt, A design strategy for mushroom-shaped microfibrils with optimized dry adhesion: Experiments and finite element analyses, J. Appl. Mech. Trans. ASME 88 (2021) 031015, http://dx.doi.org/10.1115/1.4049183.
[22] Y. Kim, C. Yang, Y. Kim, G.X. Gu, S. Ryu, Designing an adhesive pillar shape with deep learning-based optimization, ACS Appl. Mater. Interfaces 12 (2020) 24458–24465, http://dx.doi.org/10.1021/acsami.0c04123.
[23] D. Son, V. Liimatainen, M. Sitti, Machine learning-based and experimentally validated optimal adhesive fibril designs, Small 17 (2021) 2102867, http://dx.doi.org/10.1002/smll.202102867.
[24] A. Luo, A. Mohammadi Nasab, M. Tatari, S. Chen, W. Shan, K.T. Turner, Adhesion of flat-ended pillars with non-circular contacts, Soft Matter 16 (2020) 9534–9542, http://dx.doi.org/10.1039/d0sm01105c.
[25] S. Kim, M. Sitti, C.Y. Hui, R. Long, A. Jagota, Effect of backing layer thickness on adhesion of single-level elastomer fiber arrays, Appl. Phys. Lett. 91 (2007) 161905, http://dx.doi.org/10.1063/1.2801371.
[26] M. Bacca, J.A. Booth, K.L. Turner, R.M. McMeeking, Load sharing in bioinspired fibrillar adhesives with backing layer interactions and interfacial misalignment, J. Mech. Phys. Solids 96 (2016) 428–444, http://dx.doi.org/10.1016/j.jmps.2016.04.008.
[27] H. Yao, H. Gao, Mechanical principles of robust and releasable adhesion of gecko, J. Adhes. Sci. Technol. 21 (2007) 1185–1212, http://dx.doi.org/10.1163/156856107782328326.
[28] G.X. Gu, C.T. Chen, D.J. Richmond, M.J. Buehler, Bioinspired hierarchical composite design using machine learning: Simulation, additive manufacturing, and experiment, Mater. Horizons 5 (2018) 939–945, http://dx.doi.org/10.1039/c8mh00653a.
[29] Y. Mao, Q. He, X. Zhao, Designing complex architectured materials with generative adversarial networks, Sci. Adv. 6 (2020) http://dx.doi.org/10.1126/sciadv.aaz4169, eaaz4169.
[30] L. Wu, L. Liu, Y. Wang, Z. Zhai, H. Zhuang, D. Krishnaraju, Q. Wang, H. Jiang, A machine learning-based method to design modular metamaterials, Extrem. Mech. Lett. 36 (2020) 100657, http://dx.doi.org/10.1016/j.eml.2020.100657.
[31] G.X. Gu, C.T. Chen, M.J. Buehler, De novo composite design based on machine learning algorithm, Extrem. Mech. Lett. 18 (2018) 19–28, http://dx.doi.org/10.1016/j.eml.2017.10.001.
[32] Y. Kim, Y. Kim, C. Yang, K. Park, G.X. Gu, S. Ryu, Deep learning framework for material design space exploration using active transfer learning and data augmentation, Npj Comput. Mater. 7 (2021) http://dx.doi.org/10.1038/s41524-021-00609-2.
[33] D. Da, Y.C. Chan, L. Wang, W. Chen, Data-driven and topological design of structural metamaterials for fracture resistance, Extrem. Mech. Lett. 50 (2022) 101528, http://dx.doi.org/10.1016/j.eml.2021.101528.
[34] D. Shen, G. Wu, H. Il Suk, Deep learning in medical image analysis, Annu. Rev. Biomed. Eng. 19 (2017) 221–248, http://dx.doi.org/10.1146/annurev-bioeng-071516-044442.
[35] D. Amodei, S. Ananthanarayanan, R. Anubhai, J. Bai, E. Battenberg, C. Case, J. Casper, B. Catanzaro, Q. Cheng, G. Chen, J. Chen, J. Chen, Z. Chen, M. Chrzanowski, A. Coates, G. Diamos, K. Ding, N. Du, E. Elsen, J. Engel, W. Fang, L. Fan, C. Fougner, L. Gao, C. Gong, A.N. Hannun, T. Han, L.V. Johannes, B. Jiang, C. Ju, B. Jun, P. Legresley, L. Lin, J. Liu, Y. Liu, W. Li, X. Li, D. Ma, S. Narang, A. Ng, S. Ozair, Y. Peng, R. Prenger, S. Qian, Z. Quan, J. Raiman, V. Rao, S. Satheesh, D. Seetapun, S. Sengupta, K. Srinet, A. Sriram, H. Tang, L. Tang, C. Wang, J. Wang, K. Wang, Y. Wang, Z. Wang, Z. Wang, S. Wu, L. Wei, B. Xiao, W. Xie, Y. Xie, D. Yogatama, B. Yuan, J. Zhan, Z. Zhu, Deep speech 2: End-to-end speech recognition in english and mandarin, in: 33rd Int. Conf. Mach. Learn. ICML 2016, 2016, pp. 312–321.
[36] S.N. Khaderi, N.A. Fleck, E. Arzt, R.M. McMeeking, Detachment of an adhered micropillar from a dissimilar substrate, J. Mech. Phys. Solids 75 (2015) 159–183, http://dx.doi.org/10.1016/j.jmps.2014.11.004.
[37] B.N.J. Persson, M. Scaraggi, Theory of adhesion: Role of surface roughness, J. Chem. Phys. 141 (2014) 124701.
[38] B.N.J. Persson, E. Tosatti, The effect of surface roughness on the adhesion of elastic solids, J. Chem. Phys. 115 (2001) 5597–5610.
[39] H. Yao, Mechanics of robust adhesion of smooth biological attachment pads on rough surfaces, J. Adhes. Sci. Technol. 27 (2013) 775–782, http://dx.doi.org/10.1080/01694243.2012.727151.
[40] M. Abadi, P. Barham, J. Chen, Z. Chen, A. Davis, J. Dean, M. Devin, S. Ghemawat, G. Irving, M. Isard, M. Kudlur, J. Levenberg, R. Monga, S. Moore, D.G. Murray, B. Steiner, P. Tucker, V. Vasudevan, P. Warden, M. Wicke, Y. Yu, X. Zheng, Tensorflow: A system for large-scale machine learning, in: Proc. 12th USENIX Symp. Oper. Syst. Des. Implementation, OSDI 2016, 2016, pp. 265–283.
[41] I. Goodfellow, Y. Bengio, A. Courville, Deep Learning, MIT Press, 2016.
[42] C.T. Chen, G.X. Gu, Generative deep neural networks for inverse materials design using backpropagation and active learning, Adv. Sci. 7 (2020) 1902607, http://dx.doi.org/10.1002/advs.201902607.
[43] B. Sanchez-Lengeling, A. Aspuru-Guzik, Inverse molecular design using machine learning:Generative models for matter engineering, Science 361 (2018) 360–365, http://dx.doi.org/10.1126/science.aat2663.
[44] J. Peurifoy, Y. Shen, L. Jing, Y. Yang, F. Cano-Renteria, B.G. DeLacy, J.D. Joannopoulos, M. Tegmark, M. Solja˘cić, Nanophotonic particle simulation and inverse design using artificial neural networks, Sci. Adv. 4 (2018) http://dx.doi.org/10.1126/sciadv.aar4206, eaar4206.
[45] A. Carlson, H.J. Kim-Lee, J. Wu, P. Elvikis, H. Cheng, A. Kovalsky, S. Elgan, Q. Yu, P.M. Ferreira, Y. Huang, K.T. Turner, J.A. Rogers, Shear-enhanced adhesiveless transfer printing for use in deterministic materials assembly, Appl. Phys. Lett. 98 (2011) 264104, http://dx.doi.org/10.1063/1.3605558.